1372 *Inorg. Chem.* **2010**, *49*, 1372–1383
DOI: 10.1021/ic9011313

Inorganic Chemistry
Article

Mono- versus Dinuclear Pt(II) 6-(5-Trifluoromethyl-Pyrazol-3-yl)-2,2′-Bipyridine Complexes: Synthesis, Characterization, and Remarkable Difference in Luminescent Properties

Kang-Wei Wang,[†] Jing-Lin Chen,[‡,§] Yi-Ming Cheng,[†] Min-Wen Chung,[†] Cheng-Chih Hsieh,[†] Gene-Hsiang Lee,[†] Pi-Tai Chou,*[,†] Kellen Chen,[‡] and Yun Chi*[,‡]

[†]*Department of Chemistry, National Taiwan University, Taipei 106, Taiwan,* [‡]*Department of Chemistry, National Tsing Hua University, Hsinchu 300, Taiwan, and* [§]*School of Material and Chemistry Engineering, Jiangxi University of Science and Technology, Ganzhou, Jiangxi, 341000, China*

Received June 11, 2009

A series of charge-neutral mononuclear Pt(II) complexes Pt(fpbpy)(pz) (**3a**), Pt(fpbpy)(dmpz) (**4a**), Pt(fpbpy)(dbpz) (**5a**), and Pt(fpbpy)(dtfpz) (**6a**), fpbpyH = 6-(5-trifluoromethyl-pyrazol-3-yl)-2,2′-bipyridine, pzH = pyrazole, dmpzH = 3,5-dimethylpyrazole, dbpzH=3,5-di-*tert*-butylpyrazole, and dtfpzH=3,5-bis(trifluoromethyl)pyrazole, and the cationic Pt(II) dimer $[\{Pt(fpbpy)\}_2(\mu\text{-pz})]^+$ (**3b**), $[\{Pt(fpbpy)\}_2(\mu\text{-dmpz})]^+$ (**4b**), and $[\{Pt(fpbpy)\}_2(\mu\text{-dbpz})]^+$ (**5b**) were synthesized. Series **a** mononuclear complexes reveal two distinctive ligand arrangements. As unveiled by X-ray crystallography, **3a** exhibits a nearly perfect planar geometry, while structural determination on **6a** shows a perpendicular arrangement of dbpz ligand due to steric congestion. In sharp contrast, the dinuclear complexes, exemplified by **4b** and **5b**, display an intramolecular Pt···Pt separation of 3.601 and 3.403 Å, respectively. As for photophysical properties, the structural variation leads to a salient difference in emission features between **3a** (580 nm) and **6a** (510 nm). The results are rationalized by the contribution of ligand-to-ligand charge transfer and intraligand $\pi-\pi^*$ transition for **3a** and **6a** in the lowest-lying excited state, respectively. On the other hand, dinuclear complexes **3b** and **4b** reveal dual phosphorescence (denoted as P_1 and P_2 bands), for which the short wavelength emission (the P_1 band) is akin to that observed for the intraligand $\pi-\pi^*$ transition of **6a**, while the much red-shifted, broad emission (the P_2 band) is attributed to the formation of intramolecular ligand−metal-to-metal charge transfer excimer transition. Further studies of relaxation dynamics on both **3b** and **4b** showed fast excited-state equilibrium between the P_1 and P_2 bands. In contrast, only the P_2 emission band was resolved for **5b**, indicating its exergonic excimer formation. Supplementary support of the excited-state thermodynamics is also provided by time-dependent density functional theory calculations, incorporating both geometry optimized S_0 and T_1 states.

Introduction

Owing to their intriguing spectroscopic and photophysical properties as well as their promising applications in materials science, luminescent Pt(II) complexes possessing terdentate chelating chromophores have been extensively studied during the past few decades.[1,2] These terdentate ligands can be classified according to their inherent electronic characters. For example, terpyridine (terpy)[3] and its functionalized derivatives, such as 2,6-bis(pyrazolyl)pyridine (dpzpy)[4] and 2,6-bis(benzimidazol-2′-yl)pyridine (bzimpy),[5] are well-known

*Corresponding authors. E-mail: chop@ntu.edu.tw (P.-T.C.) and ychi@mx.nthu.edu.tw (Y.C.).

(1) (a) Jennette, K. W.; Gill, J. T.; Sadownick, J. A.; Lippard, S. J. *J. Am. Chem. Soc*. **1976**, *98*, 6159. (b) Ratilla, E. M. A.; Scott, B. K.; Moxness, M. S.; Kostic, N. M. *Inorg. Chem*. **1990**, *29*, 918. (c) Yip, H. K.; Che, C. M.; Zhou, Z. Y.; Mak, T. C. W. *J. Chem. Soc., Chem Commun*. **1992**, 1369. (d) Yip, H. K.; Cheng, L. K.; Cheung, K. K.; Che, C. M. *J. Chem. Soc., Dalton Trans*. **1993**, 2933. (e) Aldridge, T. K.; Stacy, E. M.; McMillin, D. R. *Inorg. Chem*. **1994**, *33*, 722. (f) Bailey, J. A.; Hill, M. G.; Marsh, R. E.; Miskowski, V. M.; Schaefer, W. P.; Gray, H. B. *Inorg. Chem*. **1995**, *34*, 4591. (g) Hill, M. G.; Bailey, J. A.; Miskowski, V. M.; Gray, H. B. *Inorg. Chem*. **1996**, *35*, 4585. (h) Arena, G.; Calogero, G.; Campagna, S.; Scolaro, L. M.; Ricevuto, V.; Romeo, R. *Inorg. Chem*. **1998**, *37*, 2763.

(2) (a) Yam, V. W.-W.; Wong, K. M.-C.; Zhu, N. *Angew. Chem., Int. Ed*. **2003**, *42*, 1400. (b) Wong, K. M.-C.; Tang, W.-S.; Chu, B. W.-K.; Zhu, N.; Yam, V. W.-W. *Organometallics* **2004**, *23*, 3459. (c) Lu, W. I.; Mi, B.-X.; Chan, M. C. W.; Hui, Z.; Che, C.-M.; Zhu, N.; Lee, S.-T. *J. Am. Chem. Soc*. **2004**, *126*, 4958. (d) Wadas, T. J.; Wang, Q.-M.; Kim, Y.-J.; Flaschenreim, C.; Blanton, T. N.; Eisenberg, R. *J. Am. Chem. Soc*. **2004**, *126*, 16841. (e) Zhang, D.; Wu, L.-Z.; Zhou, L.; Han, X.; Yang, Q.-Z.; Zhang, L.-P.; Tung, C.-H. *J. Am. Chem. Soc*. **2004**, *126*, 3440. (f) Yam, V. W.-W.; Chan, K. H.-Y.; Wong, K. M.-C.; Chu, B. W.-K. *Angew. Chem., Int. Ed*. **2006**, *45*, 6169. (g) Feng, K.; Zhang, R.-Y.; Wu, L.-Z.; Tu, B.; Peng, M.-L.; Zhang, L.-P.; Zhao, D.; Tung, C.-H. *J. Am. Chem. Soc*. **2006**, *128*, 14685. (h) Camerel, F.; Ziessel, R.; Donnio, B.; Bourgogne, C.; Guillon, D.; Schmutz, M.; Iacovita, C.; Bucher, J.-P. *Angew. Chem., Int. Ed*. **2007**, *46*, 2659. (i) Wong, K. M.-C.; Yam, V. W.-W. *Coord. Chem. Rev*. **2007**, *251*, 2477.

(3) Constable, E. C. *Chem. Soc. Rev*. **2007**, *36*, 246.

(4) Halcrow, M. A. *Coord. Chem. Rev*. **2005**, *249*, 2880.

(5) Zhang, W.; Sun, W.-H.; Zhang, S.; Hou, J.; Wedeking, K.; Schultz, S.; Froehlich, R.; Song, H. *Organometallics* **2006**, *25*, 1961.

 Published on Web 01/15/2010

for their potential to serve as neutral N-donors and, thus, for providing a versatile platform for investigating structural, absorption, and luminescent responses against external stimuli.[6] The next class of terdentate ligands is 6-phenyl-2,2′-bipyridine (phbpy) and 1,3-di-(2-pyridyl)benzene and its analogues,[7] which have been widely used in stabilizing the associated Pt(II) complexes and found to have profound photoluminescence application.[8,9] Modification of the cyclometalated diimine ligands has recently been reported via the replacement of a lateral pyridyl with a C-coordinated pyrazole moiety (cf., phpzpyH).[10] This new molecular design allows it to bind as monoanionic tridentate chelate, similar to that of the parent cyclometalated diimine, if the azole moiety remains protonated. On the other hand, the deprotonation of the 1-pyrazolyl-NH group produces a dianionic chelate. The net result may weaken the Pt···Pt interaction due to the Coulombic repulsion among the chelating ligands and, hence, reduce the probability of excimer formation. Instead, the contribution of metal-to-ligand charge transfer (^{3}MLCT) emissions from noninteracting Pt(II) unit is expected to increase.[11]

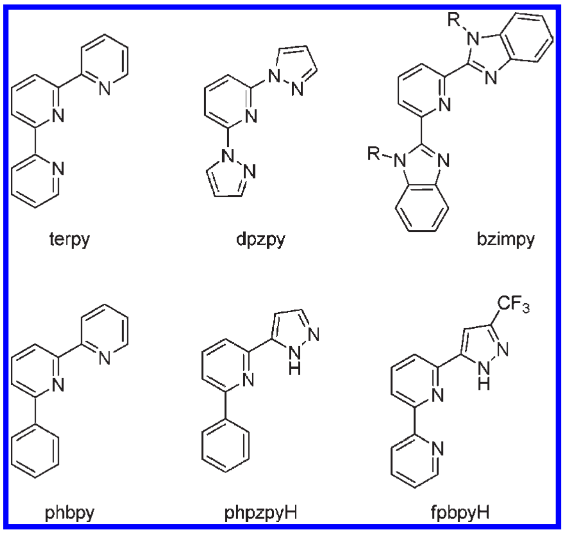

Similar to cyclometalated diimines, the third class of terdentate ligand, namely 6-(5-trifluoromethyl-pyrazol-3-yl)-2,2′-bipyridine, denoted as fpbpyH,[12] also serves as a monoanionic chelate via direct deprotonation of the pyrazolyl NH fragment, in a way similar to those of the bidentate analogues, i.e., 5-(2-pyridyl) pyrazolates.[13,14] The in situ generated fpbpy anion can then react with the metal reagent K_2PtCl_4 to afford stable Pt(II) complexes with the formula Pt(fpbpy)X (X = anionic or neutral ligand). Many of these Pt(II) complexes are found to exhibit remarkable spectroscopic and photophysical properties.[15] In addition, Pt(fpbpy)Cl also easily forms aggregates, giving a zigzag $[Pt]_n$ metal chain with a Pt···Pt distance of 3.385 Å and an interplanar separation of 3.296 Å.

Compared to d^6 octahedral metal complexes, the square-planar geometry of d^8 Pt(II) complexes permits extended substrate-binding capability at the axial, vacant coordination sites. For instance, in a series of pyrazolate-linked cyclometalated Pt(II) complexes with the general formula $[(C^\wedge N)Pt(\mu\text{-pz})]_2$ (where C^N = 2-(4,6-difluorophenyl)pyridine),[16] it is reported that the pyrazolate linkers can control the degree of metal−metal contact and the nature of the excited state through regulation of the Pt···Pt spacing.[14,17] Interestingly, due to the larger interplanar separation between the cyclometalated C^N ligands, the intramolecular $\pi-\pi$ interaction between its C^N ligands is negligible within those dimer complexes. Similar to these Pt(II) complexes bearing two bridging ligands, a number of dinuclear Pt(II) complexes containing tridentate chelating ligands have also been reported to demonstrate the effect of Pt···Pt contact on their photophysical properties.[18] The linkers used so far, in most cases, are either bidentate organic anions[19] or diphosphines

(6) (a) Chelucci, G.; Thummel, R. P. *Chem. Rev.* **2002**, *102*, 3129. (b) Baranoff, E.; Collin, J.-P.; Flamigni, L.; Sauvage, J.-P. *Chem. Soc. Rev.* **2004**, *33*, 147. (c) Castellano, F. N.; Pomestchenko, I. E.; Shikhova, E.; Hua, F.; Muro, M. L.; Rajapakse, N. *Coord. Chem. Rev.* **2006**, *250*, 1819. (d) Williams, J. A. G.; Wilkinson, A. J.; Whittle, V. L. *Dalton Trans.* **2008**, 2081. (e) Willison, S. A.; Jude, H.; Antonelli, R. M.; Rennekamp, J. M.; Eckert, N. A.; Bauer, J. A. K.; Connick, W. B. *Inorg. Chem.* **2004**, *43*, 2548. (f) Grove, L. J.; Rennekamp, J. M.; Jude, H.; Connick, W. B. *J. Am. Chem. Soc.* **2004**, *126*, 1594. (g) Yutaka, T.; Obara, S.; Ogawa, S.; Nozaki, K.; Ikeda, N.; Ohno, T.; Ishii, Y.; Sakai, K.; Haga, M. *Inorg. Chem.* **2005**, *44*, 4737.

(7) (a) Cardenas, D. J.; Echavarren, A. M.; Ramirez de Arellano, M. C. *Organometallics* **1999**, *18*, 3337. (b) Lai, S.-W.; Che, C.-M. *Top. Curr. Chem.* **2004**, *241*, 27. (c) Farley, S. J.; Rochester, D. L.; Thompson, A. L.; Howard, J. A. K.; Williams, J. A. G. *Inorg. Chem.* **2005**, *44*, 9690. (d) Kui, S. C. F.; Sham, I. H. T.; Cheung, C. C. C.; Ma, H.-W.; Yan, B.; Zhu, N.; Che, C.-M.; Fu, W.-F. *Chem.—Eur. J.* **2007**, *13*, 417.

(8) (a) Yip, J. H. K.; Suwarno, V.; Jagadese, J. *Inorg. Chem.* **2000**, *39*, 3537. (b) Zucca, A.; Doppiu, A.; Cinellu, M. A.; Stoccoro, S.; Minghetti, G.; Manassero, M. *Organometallics* **2002**, *21*, 783. (c) Yang, Q.-Z.; Wu, L.-Z.; Zhang, H.; Chen, B.; Wu, Z.-X.; Zhang, L.-P.; Tung, C.-H. *Inorg. Chem.* **2004**, *43*, 5195. (d) Young, K. J. H.; Meier, S. K.; Gonzales, J. M.; Oxgaard, J.; Goddard, W. A., III.; Periana, R. A. *Organometallics* **2006**, *25*, 4734.

(9) (a) Williams, J. A. G. *Top. Curr. Chem.* **2007**, *281*, 205. (b) Lu, W.; Roy, V. A. L.; Che, C.-M. *Chem. Commun.* **2006**, 3972. (c) Ma, D.-L.; Che, C.-M. *Chem.—Eur. J.* **2003**, *9*, 6133. (d) Che, C.-M.; Fu, W.-F.; Lai, S.-W.; Hou, Y.-J.; Liu, Y.-L. *Chem. Commun.* **2003**, 118. (e) Wong, K.-H.; Chan, M. C.-W.; Che, C.-M. *Chem.—Eur. J.* **1999**, *5*, 2845. (f) Tse, M.-C.; Cheung, K.-K.; Chan, M. C.-W.; Che, C.-M. *Chem. Commun.* **1998**, 2295. (g) Chan, C.-W.; Cheng, L.-K.; Che, C.-M. *Coord. Chem. Rev.* **1994**, *132*, 87.

(10) Koo, C.-K.; Ho, Y.-M.; Chow, C.-F.; Lam, M. H.-W.; Lau, T.-C.; Wong, W.-Y. *Inorg. Chem.* **2007**, *46*, 3603.

(11) Koo, C.-K.; Lam, B.; Leung, S.-K.; Lam, M. H.-W.; Wong, W.-Y. *J. Am. Chem. Soc.* **2006**, *128*, 16434.

(12) (a) Chen, K.; Cheng, Y.-M.; Chi, Y.; Ho, M.-L.; Lai, C.-H.; Chou, P.-T.; Peng, S.-M.; Lee, G.-H. *Chem. Asian J.* **2007**, *2*, 155. (b) Song, Y.-H.; Chiu, Y.-C.; Chi, Y.; Chou, P.-T.; Cheng, Y.-M.; Lin, C.-W.; Lee, G.-H.; Carty, A. J. *Organometallics* **2008**, *27*, 80.

(13) (a) Chi, Y.; Chou, P.-T. *Chem. Soc. Rev.* **2007**, *36*, 1421. (b) Chou, P.-T.; Chi, Y. *Chem.—Eur. J.* **2007**, *13*, 380. (c) Chou, P.-T.; Chi, Y. *Eur. J. Inorg. Chem.* **2006**, 3319. (d) Chi, Y.; Chou, P.-T. *Chem. Soc. Rev.* **2010**, DOI:10.1039/b916237b.

(14) (a) Wu, P.-C.; Yu, J.-K.; Song, Y.-H.; Chi, Y.; Chou, P.-T.; Peng, S.-M.; Lee, G.-H. *Organometallics* **2003**, *22*, 4938. (b) Chang, S.-Y.; Kavitha, J.; Li, S.-W.; Hsu, C.-S.; Chi, Y.; Yeh, Y.-S.; Chou, P.-T.; Lee, G.-H.; Carty, A. J.; Tao, Y.-T.; Chien, C.-H. *Inorg. Chem.* **2006**, *45*, 137. (c) Chang, S.-Y.; Chen, J.-L.; Chi, Y.; Cheng, Y.-M.; Lee, G.-H.; Jiang, C.-M.; Chou, P.-T. *Inorg. Chem.* **2007**, *46*, 11202. (d) Chang, S.-Y.; Kavitha, J.; Hung, J.-Y.; Chi, Y.; Cheng, Y.-M.; Li, E. Y.; Chou, P.-T.; Lee, G.-H.; Carty, A. J. *Inorg. Chem.* **2007**, *46*, 7064.

(15) Chen, J.-L.; Chang, S.-Y.; Chi, Y.; Chen, K.; Cheng, Y.-M.; Lin, C.-W.; Lee, G.-H.; Chou, P.-T.; Wu, C.-H.; Shih, P.-I.; Shu, C.-F. *Chem. Asian J.* **2008**, *3*, 2112.

(16) (a) Ma, B.; Djurovich, P. I.; Garon, S.; Alleyene, B.; Thompson, M. E. *Adv. Funct. Mater.* **2006**, *16*, 2438. (b) Ma, B.; Li, J.; Djurovich, P. I.; Yousufuddin, M.; Bau, R.; Thompson, M. E. *J. Am. Chem. Soc.* **2005**, *127*, 28.

(17) (a) Kato, M.; Sasano, K.; Kosuge, C.; Yamazaki, M.; Yano, S.; Kimura, M. *Inorg. Chem.* **1996**, *35*, 116. (b) Lai, S.-W.; Chan, M. C. W.; Cheung, K.-K.; Peng, S.-M.; Che, C.-M. *Organometallics* **1999**, *18*, 3991.

(18) (a) Sun, W.; Zhu, H.; Barron, P. M. *Chem. Mater.* **2006**, *18*, 2602. (b) Lu, W.; Chan, M. C. W.; Zhu, N.; Che, C.-M.; Li, C.; Hui, Z. *J. Am. Chem. Soc.* **2004**, *126*, 7639. (c) Lai, S.-W.; Lam, H.-W.; Lu, W.; Cheung, K.-K.; Che, C.-M. *Organometallics* **2002**, *21*, 226.

(19) (a) Lowe, G.; Ross, S. A.; Probert, M.; Cowley, A. *Chem. Commun.* **2001**, 1288. (b) Wong, K. M.-C.; Zhu, N.; Yam, V. W.-W. *Chem. Commun.* **2006**, 3441.

Scheme 1. Structural Drawings and Transformation of Pt(II) Complexes Mentioned in This Article

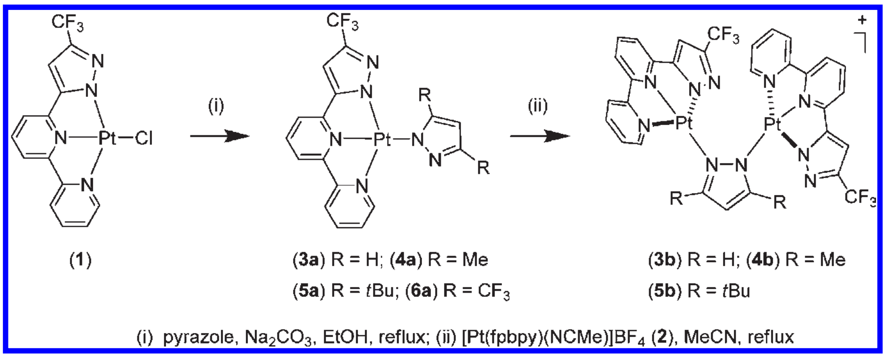

separated with distinctive carbon chain lengths.[20] Generally speaking, pyrazolate-linked Pt(II) complexes containing tridentate chelating ligands are relatively scant.[21] Moreover, to our knowledge, the utilization of a single pyrazolate linker in fine tuning the photophysical properties of Pt(II) units has not yet been reported.

Herein, we report the preparation and the structural and photophysical characteristics of a series of mono- and dinuclear Pt(II) complexes possessing the tridentate fpbpy ligand. These Pt(II) complexes show moderate to strong luminescence intensity in both fluid and solid states at room temperature and are regarded as good candidates for studying the influence of the Pt···Pt and/or $\pi-\pi$ interactions. By comparing photophysical properties between mono- and binuclear Pt(II) complexes possessing the same pyrazolate ligands as well as the substituent effect on the binuclear Pt(II) complexes linked by μ-pyrazolate bridges, we anticipate gaining more insight into the roles of the Pt···Pt and/or $\pi-\pi$ interactions with respect to the nature of the electronically excited states, particularly in terms of luminescence spectroscopy and dynamics.

Results and Discussion

Synthesis and Characterization. A general synthetic route to a series of mono- and dinuclear Pt(II) complexes containing tridentate 6-(5-trifluoromethyl-pyrazol-3-yl)-2,2′-bipyridine (fpbpyH) ligand is illustrated in Scheme 1. It is well-known that both the pyrazolate segments of the fpbpy ligand in Pt(II) complex **1** and the monodentate pyrazole ligand may be seen to act like coordinative anions via facile deprotonation of the pyrazolyl NH group in the presence of an acid scavenger. Thus, charge-neutral mononuclear Pt(II) complexes **3a**−**6a** can be synthesized by treatment of **1** with the added pyrazole in the presence of Na_2CO_3 in refluxing ethanol. However, the dmpz derivatives Pt(fpbpy)(dmpz) (**4a**) and Pt(fpbpy)(dbpz) (**5a**) were isolated only as impure samples. The impurity was caused by their rapid and partial conversion into the corresponding Pt(II) dimer complexes **4b** and **5b** during workup (see the Experimental Section). Despite this problem, respectable spectroscopic data was obtained by acquiring ^{1}H NMR spectra of the mixture and then eliminating the signals from the dinuclear Pt(II) derivatives **4b** and **5b**. In sharp contrast, the dinuclear Pt(II) complexes **4b** and **5b** were readily produced and isolated by employing exactly 0.5 equiv of dmpzH and dbpzH in refluxing ethanol. Alternative preparation of binuclear Pt(II) complex **3b** (or **4b** and **5b**) was conducted by treatment of **3a** (or **4a** and **5a**) with an equal amount of weakly stabilized [Pt(fpbpy)(NCMe)](BF_4) (**2**) in refluxing acetonitrile. The only exception was mononuclear 6a, for which the electron-withdrawing power of dtfpz ligand retarded further coordination to the second $[Pt(fpbpy)]^+$ fragment. All Pt(II) complexes were characterized by FAB-MS and NMR spectroscopy, elemental analyses, and single-crystal X-ray crystallography for **3a**, **4b**, **5b**, and **6a**.

Complex **3a** was then examined by single-crystal X-ray diffraction to establish its exact molecular structure, for which the planar arrangement of both ligands around the Pt(II) center was noted, as shown in Figure 1. The Pt−N(5) bond length in **3a** (2.009(5) Å) is comparable to that of the dimer [Pt_2(6-phenyl-2,2′-bipyridine)$_2$(μ-pz)](PF_6) (2.009(4) Å).[22] In addition, short intramolecular N···H contacts were observed between fpbpy and pz ligands, N(6)···H(1) = 2.196 and N(4)···H(15) = 2.383 Å, which was supported by the downfield ^{1}H NMR signals observed at δ 10.54 and 8.44 attributed to the H(1) and H(15) atoms of **3a**, respectively. Furthermore, complex **3a** was stacked in a head-to-tail fashion along the *a* axis, with alternating short and long Pt···Pt distances of 3.419 and 4.526 Å as well as the Pt−Pt−Pt angle of 136°. The intermolecular separations between the fpbpy ligands were about 3.345 and 3.355 Å, respectively. Similar patterns were also observed in the crystal structures of several dimeric Pt(II) complexes linked by weak Pt···Pt bonding interaction.[23] Nevertheless, due to the long interacting distance in an antiparallel configuration, the $\pi-\pi$ stacking, if it even exists, must be rather weak or even negligible (vide infra).

For a direct comparison, single-crystal X-ray structural analysis of the dtfpz substituted **6a** was also conducted, for which the ORTEP diagram is shown in Figure 2. Even though the dfpz ligand in **6a** was highly electron deficient, the Pt−N(5) distance of 2.019(7) Å in **6a** was essentially identical to that of **3a** (2.009(5) Å), after taking experimental error into consideration. In addition, the [Pt(fpbpy)] and pyrazolate fragments in **6a** were twisted against each other

(20) (a) Lai, S.-W.; Cheung, T.-C.; Chan, M. C. W.; Cheung, K.-K.; Peng, S.-M.; Che, C.-M. *Inorg. Chem.* **2000**, *39*, 255. (b) Lu, W.; Zhu, N.; Che, C.-M. *Chem. Commun.* **2002**, *8*, 900.
(21) Bailey, J. A.; Miskowski, V. M.; Gray, H. B. *Inorg. Chem.* **1993**, *32*, 369.
(22) Lai, S.-W.; Chan, M. C.-W.; Cheung, T.-C.; Peng, S.-M.; Che, C.-M. *Inorg. Chem.* **1999**, *38*, 4046.
(23) (a) Wadas, T. J.; Wang, Q.-M.; Kim, Y.-J.; Flaschenreim, C.; Blanton, T. N.; Eisenberg, R. *J. Am. Chem. Soc.* **2004**, *126*, 16841. (b) Buss, C. E.; Mann, K. R. *J. Am. Chem. Soc.* **2002**, *124*, 1031. (c) Crowley, J. D.; Steele, I. M.; Bosnich, B. *Inorg. Chem.* **2005**, *44*, 2989.

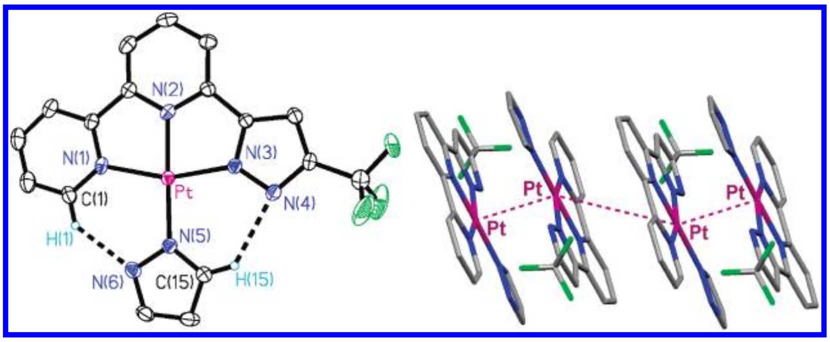

Figure 1. ORTEP drawing of **3a**, showing the atom labeling scheme with 30% thermal ellipsoids and the side-view that depicted the molecular packing in the crystal lattices; selected bond lengths: Pt−N(1) = 2.048(5), Pt−N(2) = 1.950(5), Pt−N(3) = 2.004(5), Pt−N(5) = 2.009(5), N(6)···H(1) = 2.196, and N(4)···H(15) = 2.383 Å, and intermolecular Pt···Pt distances = 3.419 and 4.526 Å.

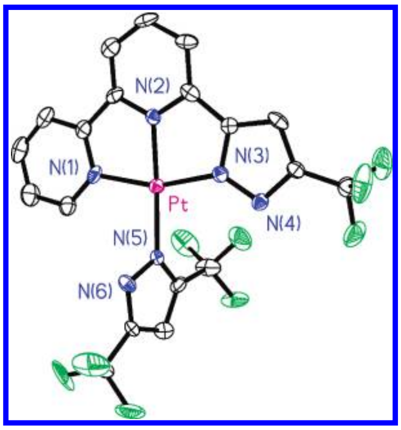

Figure 2. ORTEP drawing of **6a**, showing the atom labeling scheme with 30% thermal ellipsoids; selected bond lengths: Pt−N(1) = 2.029(7), Pt−N(2) = 1.943(7), Pt−N(3) = 1.979(8), and Pt−N(5) = 2.019(7) Å.

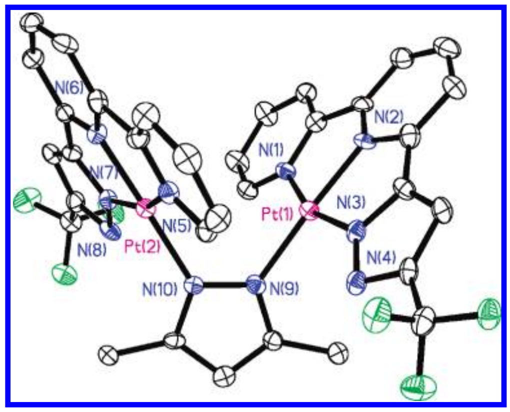

Figure 3. ORTEP drawing of the Pt(II) cation in **4b** showing the atom labeling scheme with 30% thermal ellipsoids; selected bond lengths: Pt(1)−N(1) = 2.011(9), Pt(1)−N(2) = 1.944(9), Pt(1)−N(3) = 1.983(8), Pt(1)−N(9) = 2.025(9), Pt(2)−N(5) = 2.023(9), Pt(2)−N(6) = 1.945(8), Pt(2)−N(7)=2.003(8), Pt(2)−N(10)=2.020(8), and Pt(1)···Pt(2)=3.601 Å.

and had a dihedral angle of 76.9°, due to the large steric interaction imposed by the same CF_3 groups. As a result, both the intermolecular $\pi-\pi$ stacking interactions between the two fpbpy ligands and the nonbonding Pt···Pt interaction were prohibited.

As for the structural analysis of **4b** (Figure 3), both Ir(I) and Pt(II) d^8 transition-metal elements linked by azolate fragments have been well documented in the literature, showing their behavior as effective bridging ligands.[24] Naturally, the metric parameters of each [Pt(fpbpy)] moiety in **4b** showed negligible differences from those determined in mononuclear **3a** and **6a**, but they were joined by a bridging pyrazolate with an interplanar angle of 24.5°. The observed Pt···Pt distance of 3.601 Å is comparable to that of $[Pt_2$(6-phenyl-2,2′-bipyridine$)_2$-(μ-pz)](PF_6) (3.612(2) Å),[22] but both distances are longer than those expected with significant Pt−Pt interaction.[25]

The growth of single crystals of **5b** that possessed a smaller counteranion BF_4^- unfortunately failed. To further explore the effect of the pyrazolate linker, particularly its influence on the Pt···Pt interaction within the dimeric [Pt(fpbpy)] units, we, thus, carried out single-crystal X-ray structural determination on a metathetical derivative $[\{Pt(fpbpy)\}_2(\mu\text{-dbpz})](CF_3SO_3)$ (**5b**). As depicted in Figure 4, complex **5b** showed an identical skeletal arrangement for the cationic Pt(II) fragment versus that of the dmpz complex **4b**. However, the Pt···Pt nonbonding distance in **5b** was notably shorter

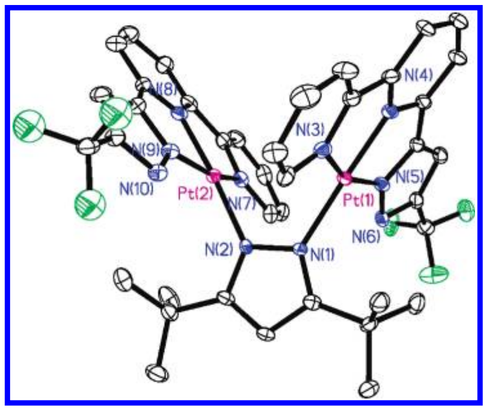

Figure 4. ORTEP drawing of the Pt(II) cation in **5b** showing the atom labeling scheme with 30% thermal ellipsoids; selected bond lengths: Pt(1)−N(1) = 2.024(6), Pt(1)−N(3) = 2.023(7), Pt(1)−N(4) = 1.948(6), Pt(1)−N(5) = 2.007(6), Pt(2)−N(2) = 2.015(6), Pt(2)−N(7) = 2.024(6), Pt(2)−N(8) = 1.951(6), Pt(2)−N(9) = 1.998(6), and Pt(1)···Pt(2) = 3.403 Å.

(24) (a) Tejel, C.; Ciriano, M. A.; Millaruelo, M.; Lopez, J. A.; Lahoz, F. J.; Oro, L. A. *Inorg. Chem.* **2003**, *42*, 4750. (b) Umakoshi, K.; Yamauchi, Y.; Nakamiya, K.; Kojima, T.; Yamasaki, M.; Kawano, H.; Onishi, M. *Inorg. Chem.* **2003**, *42*, 3907. (c) Falvello, L. R.; Fornies, J.; Martin, A.; Sicilia, V.; Villarroya, P. *Organometallics* **2002**, *21*, 4604. (d) Fang, C.-H.; Chen, Y.-L.; Yang, C.-H.; Chi, Y.; Yeh, Y.-S.; Li, E. Y.; Cheng, Y.-M.; Hsu, C.-J.; Chou, P.-T.; Chen, C.-T. *Chem.—Eur. J.* **2007**, *13*, 2686.

(25) (a) Miskowski, V. M.; Houlding, V. H. *Inorg. Chem.* **1991**, *30*, 4446. (b) Houlding, V. H.; Miskowski, V. M. *Coord. Chem. Rev.* **1991**, *111*, 145. (c) Connick, W. B.; Henling, L. M.; Marsh, R. E.; Gray, H. B. *Inorg. Chem.* **1996**, *35*, 6261. (d) Connick, W. B.; Marsh, R. E.; Schaefer, W. P.; Gray, H. B. *Inorg. Chem.* **1997**, *36*, 913.

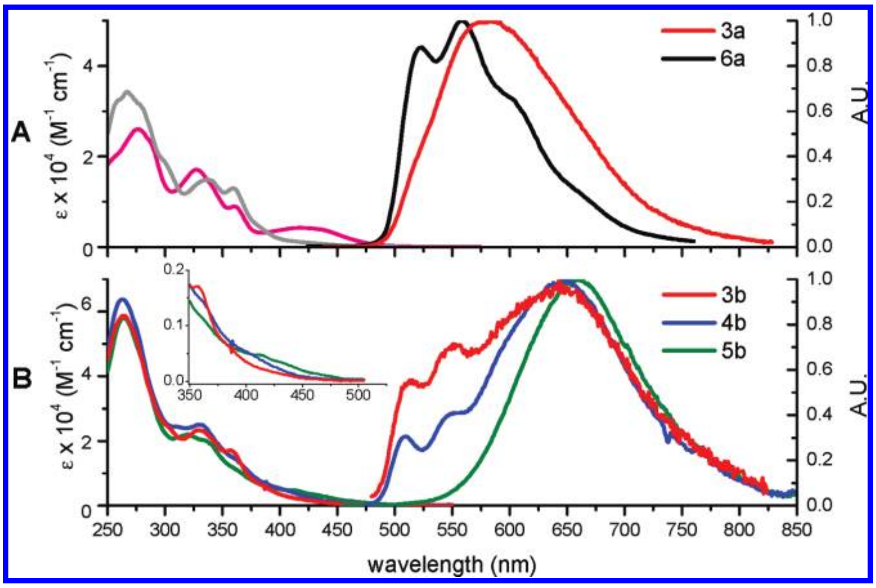

Figure 5. (A) UV−vis absorption and emission spectra of mononuclear Pt(II) complexes **3a** and **6a** in CH_2Cl_2 at room temperature, and (B) respective spectra of dinuclear Pt(II) complexes **3b**−**5b**. Inset: the expanded absorption spectra of **3b**−**5b** in CH_2Cl_2 between the region of 350−500 nm. For emission study, the concentration prepared for all titled complexes is ∼1.0−2.0 × 10^{-5} M, with λ_{ex} ∼350 nm.

Table 1. Photophysical Properties of the Studied Pt(II) Complexes in CH_2Cl_2 Solution

	λ_{abs}(nm) ($\varepsilon \times 10^3 M^{-1}cm^{-1}$)	λ_{em}(nm)	τ_{obs}(ns)	$\Phi_{em}{}^{a}$	k_r	k_{nr}
3a	277(26), 328(17), 360(9.0), 419(4.2)	582	1 257	0.045	3.6×10^4	7.6×10^5
6a	267(34), 337(13), 359(12)	523, 558	6 133	0.28	4.6×10^4	1.2×10^5
3b	264(59), 330(23), 356(17)	515, 551, 643	27.0	0.005[a]	1.9×10^5	3.7×10^6
4b	263(64), 330(25)	509, 551, 648	287	0.05[a]	1.7×10^5	3.3×10^6
5b	264(58), 320(22), 420(4.2)	655	630	0.14[a]	2.2×10^5	1.4×10^6

[a] Quantum yield is calculated by the integration of P_1 and P_2 bands.

(3.403 versus 3.601 Å) due to an increased steric effect exerted by the bulky 3,5-di-*tert*-butylpyrazolate bridge. For further comparison, this Pt···Pt separation is still comparable to the typical nonbonding contact observed in other classes of Pt(II) linear-chain structures (3.09−3.50 Å).[25] We, thus, expect the possibility of intramolecular Pt···Pt interaction, especially in the electronically excited state (vide infra) as well as the feasibility of fine-tuning the molecular structure by altering substituents.

Photophysical Properties. The absorption and emission spectra in CH_2Cl_2 at 298 K are shown in Figure 5, while pertinent photophysical data are summarized in Table 1. Comparing most of the Pt(II) complexes possessing anionic terdentate chelates, the absorption spectra of all complexes can basically be ascribed to a few main domains in terms of the magnitude of absorption coefficients, together with the molecular orbital analysis based on time-dependent DFT (TD-DFT) calculations (vide infra). In Figure 5A, the intense absorption bands of series **a** complexes in the higher energy region (< 300 nm), with an extinction coefficient (ε) on the order of ∼10^4 M^{-1} cm^{-1}, most probably originated from the intraligand π−π* transitions. The moderately intense band at 300−380 nm, with ε on the order of ∼10^3 M^{-1} cm^{-1}, can be tentatively assigned to the ligand-to-ligand charge transfer (LLCT) transition. The lower energy absorption bands around 380−500 nm for **3a**, as assigned according to those documented in literature[26] and in a later computational approach, originated from the metal-to-ligand (bpy) charge transfer transitions (MLCT) mixed mainly with ancillary pz(π) → tridentate fpbpy(π*) LLCT transition, while those for **6a** are assigned to MLCT in combination with an intraligand π−π* transition mainly associated with the fpbpy moiety. Experimentally, the difference in transition properties between **3a** and **6a** can be supported by the relatively much larger S_0−S_1 absorption coefficient (e.g., ∼2 × 10^4 $M^{-1}cm^{-1}$ at 420 nm) for **3a** compared to ∼4 × 10^3 $M^{-1}cm^{-1}$ (420 nm) for **6a**. Such a difference, in a qualitative manner, could be rationalized by the geometry variation, in which **3a** is virtually planar between the pz and fpbpy ligands, such that pz(π) → fpbpy(π*) LLCT is allowed due to an efficient π-electron overlap/delocalization. Conversely, CF_3 (**6a**) substitution makes ancillary pz tilted significantly with respect to the fpbpy chromophore. In the case of **6a**, these two ligands are staggered with an interplanar angle of 76.9° due to a steric interaction imposed by the CF_3 groups (vide supra). As a result, the nonplanar configuration between the fpbpy and the CF_3 substituted pyrazolate would lead to the virtually less allowed pz(π) → fpbpy(π*) ligand-to-ligand transition for **6a**. Instead, the lowest-lying transition for **6a** is dominated by the intraligand π−π* transition associated with the fpbpy chelate. Further discussion will be presented in the following sections on emissions and computation.

Figure 5A also depicts the emission spectra of the series **a** complexes in room temperature CH_2Cl_2 solution, while

(26) Lu, W.; Chan, M. C. W.; Cheung, K.-K.; Che, C.-M. *Organometallics* **2001**, *20*, 2477.

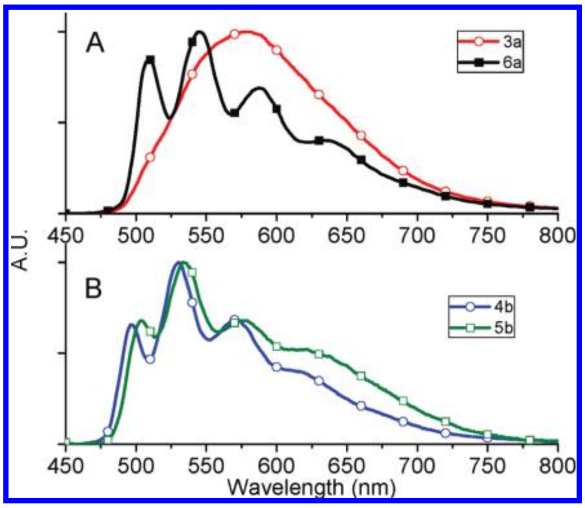

Figure 6. Solid-state emission spectra of the crystalline samples of **3a** and **6a** (A) and **4b** and **5b** (B) at room temperature with $\lambda_{ex} \sim 350$ nm; *a* < 400 nm cutoff filter has been placed in front of the entrance of monochromator.

pertinent steady-state and dynamics data are listed in Table 1. For all emission bands of these studied complexes, the deduced radiative decay time τ_r ($\tau_r = 1/k_r$) of > μs (see Table 1), together with their significant O_2 quenching, indicates their origin in phosphorescence. Complex **3a** exhibits a smooth and broad emission with a peak maximized at ~580 nm, while **6a** shows blue-shifted emissions (cf. **3a**) with notable vibronic progressions and 0−0 onset at ~510 nm. For **3a**, the planar relationship between pz and fpbpy increases the pz → fpbpy contribution to the lowest-lying transition (T_1 state). Accordingly, the emission becomes structureless (cf. **6a**) due to its incorporating a great percentage of ligand-to-ligand charge transfer (LLCT) transition. Conversely, the less allowed pz → fpbpy transition and, hence, the more intraligand (fpbpy) $\pi\pi^*$ transition render more vibronic progressive emission for **6a**. This spectral feature manifests the difference, per se, between **3a** and **6a** regarding the lowest-lying transition properties, consistent with the viewpoint drawn on the above discussion regarding absorption spectra.

The emission spectrum of **3a** shows negligible concentration and temperature dependence within 10^{-6}−10^{-3} M, despite its nearly planar geometry (see Figures S1−S2 in Supporting Information). The lack of intermolecular interaction may be rationalized by the interference of the bulky CF_3 group in the fpbpy moiety. Note that even in the solid crystal, as revealed by the X-ray structural analysis (vide supra), π-stacking in **3a** is rather weak, and the ancillary pz in one **3a** lies on top of the fpbpy of the adjacent molecule to minimize the π-stacking effect. This viewpoint can be further supported by the notable emission signal of **3a** in the solid state. As depicted in Figure 6A, the crystalline sample of **3a** exhibits a unique, broadband maximized at ~580 nm, the spectral features of which are similar to that observed in a CH_2Cl_2 solution (cf. Figure 5A). Complex **6a** also lacks concentration dependence in both absorption and emission spectra in CH_2Cl_2 (within 10^{-6}−10^{-3} M). Its emission (Figure 6A) in the crystalline sample, in view of the peak wavelengths and the vibronic spectral feature, is more or less the same as that in solution (CH_2Cl_2), providing sufficient evidence that the intermolecular π−π stacking interaction between the two fpbpy ligands as well as the nonbonding Pt···Pt interaction are prohibited due to the mutually twisted pyrazolate fragments in **6a** (vide supra).

As for series **b** dinuclear complexes (see Figure 5B), due to the nearly orthogonal arrangement between the Pt-(fpbpy) segments and the bridging pyrazolate, complexes **3b** and **4b** exhibit a UV/vis spectral pattern similar to that of series **a** mononuclear counterparts; thus, the corresponding assignments of absorption spectra are qualitatively the same. Nevertheless, due to the dual fpbpy moieties, a significant increase of the absorption extinction coefficient is observed throughout the spectral range of 250−450 nm (cf. Figure 5A and B). Moreover, there is no appreciable red shift of the lower-lying absorption bands for **3b** (or **4b**) versus their mononuclear counterparts. The result indicates that the intramolecular Pt(fpbpy)−Pt(fpbpy) interaction, if it even exists, must be too weak to cause changes of electronic configuration in the ground state. However, this may not be the case for **5b**, which showed an additional lower energy absorption shoulder at about 420 nm (see the insert of Figure 5 B), implying that the *tert*-butyl steric effect brings the two Pt(II) atoms even closer together, such that the intramolecular Pt···Pt contact may not be fully negligible in **5b** in the ground state.

In contrast to series **a** complexes, **3b** and **4b** in CH_2Cl_2 solution reveal notable dual emission. The short wavelength emission, denoted as the P_1 band, with characteristic vibronic progression maximized at ~510 nm for both **3b** and **4b**, is reminiscent of that of **6a**, possessing a nonplanar framework. The long wavelength emission, denoted as the P_2 band, is broad and structureless, having peak wavelengths at 642 and 648 nm for **3b** and **4b**, respectively. Similar excitation spectra were obtained by monitoring at both P_1 (e.g., 510 nm) and P_2 (e.g., 700 nm) emission regions of **3b** and **4b**, supporting their identical ground-state origin (see Figure S3 in the Supporting Information). While the P_1 band can be unambiguously assigned to a regular Franck−Condon type of emission that is mirror imaged to the absorption, the much red-shifted emission, denoted as the P_2 band, is tentatively attributed to the ligand (π^*)−metal-to-metal (d_π) charge transfer (^{3}LMMCT) excimer emission. Since the ratio of intensity for P_2 versus P_1 is concentration independent, the possibility of a dual emission originating from the intermolecular interaction can be ruled out. Instead, a more plausible mechanism could be the intramolecular excimer formation via a dual Pt(fpbpy) interaction in the electronically excited state.[16b] As for complex **5b**, only the P_2, or excimer, emission band was resolved at 655 nm in CH_2Cl_2, indicating the perhaps highly exergonic reaction for the excimer formation due to the closest Pt···Pt distance and, hence, the strongest interaction (vide supra). Since the intramolecular Pt···Pt distance is sufficiently long (e.g., 3.601 Å in **4b**), the excimer formation may require a large amplitude bending motion for each Pt fragment. This viewpoint can be supported by the emission spectra of **4b** and **5b** in the solid state, which reveals dominant normal emission bands (P_1 band) maximized at 530 and 534 nm, respectively (see Figure 6), due to the prohibition of a large amplitude Pt···Pt motion in the solid state.

Scheme 2. Proposed Fast Equilibrium between Both the Dinuclear Monomer and Excimer Formation for **3b** and **4b**[a]

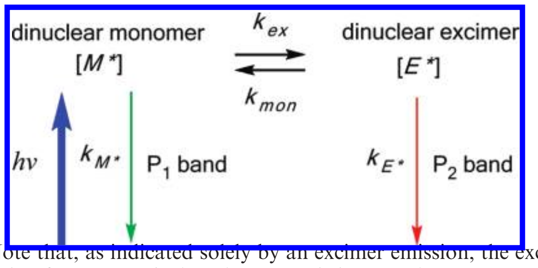

[a] Note that, as indicated solely by an excimer emission, the excimer formation for **5b** must be largely exergonic in CH_2Cl_2.

Monitoring the emission from 500 to 800 nm, independent of the origin of emission, revealed that the decay time constants of P_1 and P_2 bands were identical for either **3b** or **4b**. For example, a single decay time of 27 ± 2 ns for both P_1 and P_2 bands was resolved for **3b**. Likewise, lifetimes of P_1 and P_2 bands, within experimental error, were within 287 ± 13 ns for **4b** in a degassed CH_2Cl_2 solution (see Table 1). For **5b**, a decay time constant of 630 ± 31 ns was resolved for the P_2 emission in CH_2Cl_2. Upon monitoring at the P_2 band (e.g., 700 nm) for all **3b**−**5b**, no rise time components could be resolved by the current time-correlated single-photon counting system, for which the response time is ~300 ps. These results lead us to propose the coupled reaction dynamics depicted in Scheme 2.

In Scheme 2, k_{ex} and k_{mon} denote the intramolecular excimer formation and dissociation rate constants, respectively; k_{M^*} and k_{E^*} represent the population decay rate constants for dinuclear monomer and excimer in the excited state (T_1). As a result, the time-dependent concentration for monomer ([M*]) and excimer ([E*]) at their T_1 state can be expressed as

$$[\mathrm{M}*] = [\mathrm{M}*]_0(\alpha_1^{\mathrm{M}*}\, e^{-t/\tau_1} + \alpha_2^{\mathrm{M}*}\, e^{-t/\tau_2})$$

$$[\mathrm{E}*] = [\mathrm{M}*]_0(\alpha_1^{\mathrm{E}*}\, e^{-t/\tau_1} + \alpha_2^{\mathrm{E}*}\, e^{-t/\tau_2})$$

$$\alpha_1^{\mathrm{M}*} = \frac{\gamma_{\mathrm{M}*} - \gamma_2}{\gamma_1 - \gamma_2}, \quad \alpha_2^{\mathrm{M}*} = \frac{\gamma_1 - \gamma_{\mathrm{M}*}}{\gamma_1 - \gamma_2}, \quad -\alpha_1^{\mathrm{E}*} = \alpha_2^{\mathrm{E}*}$$

$$\gamma_1, \gamma_2 = \tau_1^{-1}, \tau_2^{-1} = \frac{1}{2}\{(\gamma_{\mathrm{M}*} + \gamma_{\mathrm{E}*}) \pm [(\gamma_{\mathrm{M}*} - \gamma_{\mathrm{E}*})^2 + 4k_{\mathrm{ex}}k_{\mathrm{mon}}]^{1/2}\}$$

$$\gamma_{\mathrm{M}*} = \gamma_2 + \alpha_1^{\mathrm{M}*}(\gamma_1 - \gamma_2) = k_{\mathrm{M}*} + k_{\mathrm{ex}},$$
$$\gamma_{\mathrm{E}*} = \gamma_1 - \alpha_1^{\mathrm{M}*}(\gamma_1 - \gamma_2) = k_{\mathrm{E}*} + k_{\mathrm{mon}}$$

Supported by the ≪300 ps rise time and much longer population decay time (≫ tens of nanoseconds), it is reasonable to assume $k_{\mathrm{ex}}, k_{\mathrm{mon}} \gg k_{\mathrm{M}*}, k_{\mathrm{E}*}$, such that $\gamma_{\mathrm{M}*} \cong k_{\mathrm{ex}}$, $\gamma_{\mathrm{E}*} \cong k_{\mathrm{mon}}$. This gives the time constant of the rise component of excimer (E*) to be $\gamma_1 = k_{\mathrm{ex}} + k_{\mathrm{mon}}$, while the decay time constant for both $k_{\mathrm{M}*}$ and $k_{\mathrm{E}*}$ are equal, which is deduced to be $\gamma_2 = k_{\mathrm{E}*}\left(\frac{k_{\mathrm{ex}}}{k_{\mathrm{ex}} + k_{\mathrm{mon}}}\right) + k_{\mathrm{M}*}\left(\frac{k_{\mathrm{mon}}}{k_{\mathrm{ex}} + k_{\mathrm{mon}}}\right)$. This reaction scheme, thus, concludes a very fast excited-state equilibrium between P_1 and P_2 bands, for which the time constant (≪300 ps) cannot be resolved at the current stage.

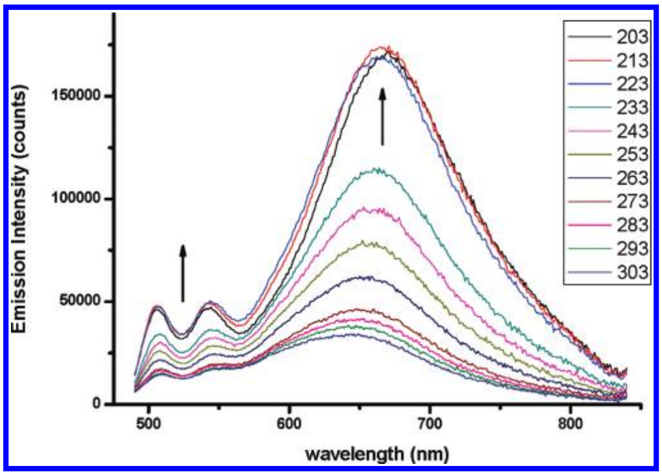

Figure 7. Temperature-dependent emission spectra of **4b** (1.2×10^{-5} M) recorded in a CH_2Cl_2 solution from 303 to 203 K.

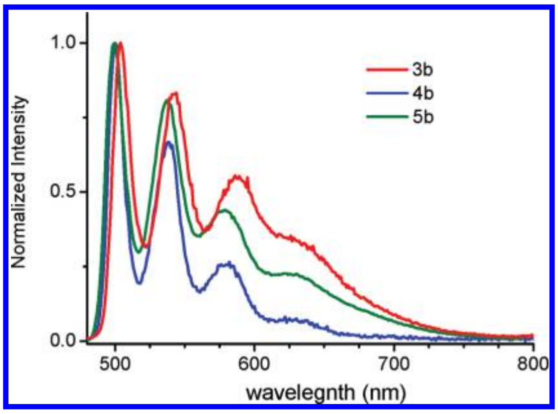

Figure 8. Emission spectra of complexes **3b**, **4b**, and **5b** in a CH_2Cl_2 solvent matrix at 77K (~1.0×10^{-5} M).

We then performed temperature-dependent studies in an attempt to gain more insight into the correlation between P_1 and P_2 bands. Unfortunately, as shown in Figure 7, for e.g. **4b**, the results are rather complicated. Nevertheless, as for a general trend, upon decreasing the temperature from 303 to 203 K in CH_2Cl_2, all peak intensities of the P_1 and P_2 bands were increased, while growth of the P_2 intensity was apparently faster than that of the P_1 band. The dynamics of relaxation showed increases of the observed lifetimes for both the P_1 and P_2 bands from 287 ± 13 to 355 ± 15 ns upon decreasing the temperature from 298 to 203 K, indicating that the nonradiative decay rate constant k_{nr} also changed significantly with temperature. The decay dynamics at each temperature are provided in Table S1 of the Supporting Information. The same decay time constants were found for boththe P_1 and P_2 bands, which is consistent with the proposed mechanism of fast equilibrium between the monomer and the excimer. Moreover, further lowering the temperature close to the freezing point of CH_2Cl_2 (178 K (−95 °C)) caused abrupt changes in the viscosity, which prohibited the excimer formation drastically (not shown here). At 77 K, all series **b** complexes show unique, normal structured emission bands around 500−550 nm, with a lack of broad excimer emission at longer wavelengths

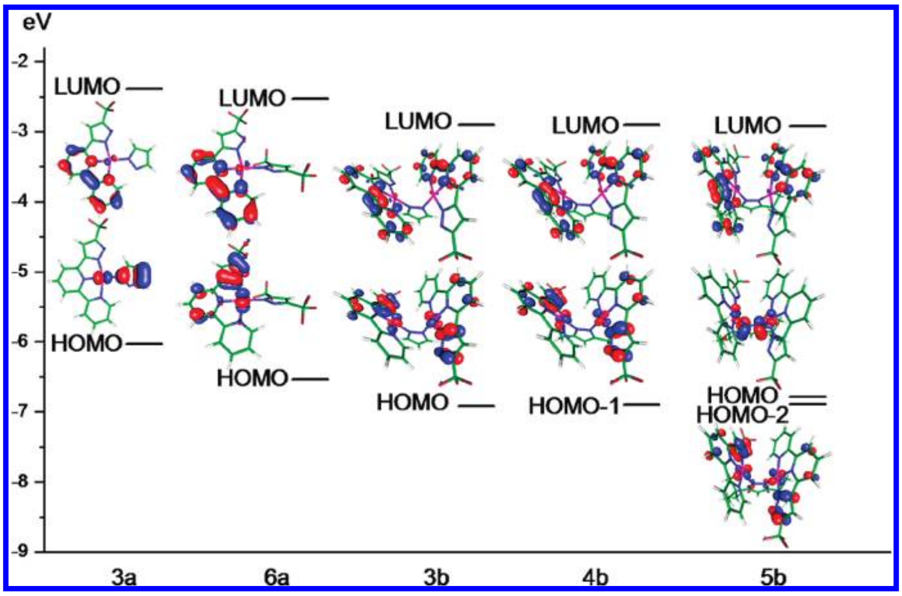

Figure 9. Schematic representation of the calculated electronic structure and the frontier orbitals in the gas phase for all Pt(II) complexes at their S_0-optimized geometries. Also shown are the isodensity surface contours of the involved frontier orbitals.

Table 2. Calculated Energy Levels and Orbital Transition Analyses of the Series **a** and **b** Pt(II) Complexes[a,b]

series **a**	state	λ_{cal} (nm)	*F*	assignments	series **b**	state	λ_{cal} (nm)	*f*	assignments
3a	T_1	614.2 (490.8)	0	HOMO → LUMO (93%)	**3b**	T_1	635 (467.5)	0	HOMO → LUMO (90%)
	S_1	428.1	0.0818	HOMO → LUMO(93%)		S_1	432.4	0.0012	HOMO → LUMO(58%) HOMO-1 → LUMO+1(26%)
6a	T_1	634 (475.3)	0	HOMO → LUMO (95%)	**4b**	T_1	635.2 (468.2)	0	HOMO → LUMO (89%)
	S_1	407.1	0.0041	HOMO → LUMO (90%)		S_1	434.2	0.0001	HOMO-1 → LUMO(51%) HOMO-3 → LUMO+1(20%) HOMO → LUMO(13%)
					5b	T_1	635.6 (469.9)	0	HOMO → LUMO (87%)
						S_1	434.8	0.0024	HOMO-2 → LUMO(36%) HOMO → LUMO(36%) HOMO-3 → LUMO+1(14%)

[a] Absorption in the singlet manifold was calculated based on the optimized S_0 geometry, while the triplet manifold was calculated based on the optimized T_1 geometry, followed by $T_1 \rightarrow S_0$ transition. [b] Data shown in parentheses are the $S_0 \rightarrow T_1$ transitions calculated based on the optimized ground-state geometries (S_0).

(see Figure 8). This is consistent with the freezing of the required large amplitude vibrational motion. Moreover, the temperature-dependent k_{nr}, in combination with the viscosity dependence on the relaxation dynamics/excimer kinetics, makes the extraction of thermodynamic and dynamic parameters infeasible. Thus, detailed kinetic/thermodynamic approaches were not further pursued in this study.

Such an intramolecular excimer formation requires a relatively large amplitude motion to bring the two Pt(fpbpy) chromophores close enough to induce, e.g., Pt···Pt or $\pi-\pi$ stacking interactions. Supplementary support of this proposal is provided by the computational approaches. TD-DFT calculations for the transition in the lowest-lying singlet and triplet manifolds were performed based on the respective geometry optimized structure, together with the consideration of the solvation effect (e.g., CH_2Cl_2, see Experimental Section). Vibrational frequencies were then calculated based on their optimized geometries to verify that each of the calculated geometries was the global optimized structure. Figure 9 depicts selected frontier orbitals that are mainly involved in the low-lying transitions. The description of frontier orbitals involved in the transitions and the corresponding energy gaps for all complexes are listed in both Figure 9 and Table 2. As listed in Table 2, the excitations of both lowest singlet and triplet excited states (S_1 and T_1) of **3a** and **6a**, for the most part, are attributed to the highest occupied molecular orbital (HOMO) to the lowest unoccupied molecular orbital (LUMO) transition. Nevertheless, the greatly different character of HOMOs suggests the possession of different transition characters. As depicted in Figure 9, the HOMO of **3a** is localized at the pyrazolate moiety, and the central metal atom, such that S_1 (T_1) is associated with a dominant LLCT transition mixed with a MLCT transition [d_π (Pt) → π^* (fpbpy)]. Conversely, the HOMO of **6a** is greatly distributed within the pyrazolate segment of a tridentate fpbpy chelate, and its lowest-lying transition is primarily ascribed to a fpbpy intraligand $\pi-\pi^*$ transition mixed to a minor extent with

MLCT. The properties of the LLCT for **3a** and the intraligand $\pi-\pi^*$ for **6a** clearly distinguish their respective structureless and vibronic progressive emission features (vide supra). As for dinuclear **b** complexes, though a bit complicated in view of the contribution of frontier orbitals, the calculated $S_0 \rightarrow S_1$ and $S_0 \rightarrow T_1$ transitions are mainly contributed to the fpbpy intraligand $\pi-\pi^*$ transition mixed to a slight extent with MLCT (d_π(Pt) $\rightarrow \pi^*$(fpbpy); see both Figures 9 and Table 2. For **3b** and **4b**, the calculated lower-lying transitions match well with respect to the experimental results. For example, the S_1 states of **3b** and **4b** are all calculated to be around ~430 nm, the value of which is close to the observed onsets of < 480 nm of the absorption spectra recorded in a CH_2Cl_2 solution.

Geometry optimization at the T_1 state and calculation of the $T_1 \rightarrow S_0$ transition revealed that the Franck–Condon emission for **3a** was estimated to be ~614 nm, which is qualitatively close to the phosphorescence maximum of 580 nm. However, the calculated $T_1 \rightarrow S_0$ transition of 634 nm for **6a** was not only much deviated from the observed phosphorescence (550 nm) but also opposite of the experimental trend observed for **3a** and **6a**. In yet another approach, with geometry optimization at the S_0 state and calculation of the $S_0 \rightarrow T_1$ transition, for **3a**, the calculated T_1 energy of 490 nm was lower than that of **6a** (475 nm, see also Table 2), consistent with the corresponding emission gap (see Figure 5). Also, the calculated energy gaps of the T_1 states of **3b** (467.5 nm) and **4b** (468.2 nm) were qualitatively in agreement with the blue-edge of their respective P_1 phosphorescence spectra recorded in a CH_2Cl_2 solution. These results indicate that the TD-DFT calculation, based on the geometry optimized ground state, works better in predicting the lowest Franck–Condon excited state for both absorption and emission. We, thus, suspect that the emission gap, estimated via $T_1 \rightarrow S_0$, vertical excitation may be subject to an ill-defined Franck–Condon transition. This issue is pending future resolution. For **5b**, because there is a close match between the calculated S_1 and the corresponding absorption (see Table 1), we also have confidence in the calculated normal T_1 state of 469.9 nm (Table 2), even though the normal phosphorescence cannot be resolved due to the exergonic excimer formation in **5b** (vide supra).

Although Pt–Pt bimetallic interaction is a key role to the excimer formation, the possible role that the $\pi-\pi$ stacking played in stabilizing the excimer formation has to be examined. To gain more insight into this issue, we further performed constrained optimization at each Pt···Pt distance to scan the potential energy surface of **5b** from the geometry optimized T_1 states. Because the traditional DFT methods cannot estimate the dispersion interactions well,[27] we alternatively applied DFT-D methodology[28] with the meta-generalized gradient approximation (GGA) exchange–correlation functional TPSS.[29] The TPSS function was modified by adding an empirical damping function to correct the description of

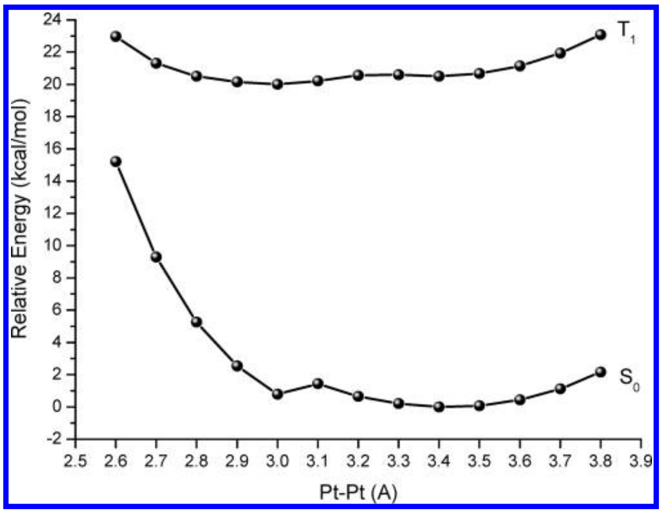

Figure 10. Potential energy surface scan of the S_0 and T_1 states of **5b** versus the Pt···Pt distance. The geometries of the S_0 and T_1 states at various Pt···Pt distances were performed with the restricted and unrestricted TPSS methods, respectively. Note that in each scan, except for the fixed Pt···Pt distance, all other ligands are freely optimized.

the dispersion interaction; the results could better match that of the MP2 method. In this approach, except for the fixed Pt···Pt distance in each scan, all the other ligands are freely optimized such that any other interactions, e.g. ligand–ligand $\pi-\pi$ stacking, have been intrinsically considered. As shown in Figure 10, the results for **5b** reveal two local minima at the S_0 state separated by a small barrier of ~1.45 kcal/mol (~ 500 cm^{-1}). One local minimum is similar to the nonbonding Pt···Pt distance of ~3.4 Å obtained from X-ray structural determination; the other is at ~3.0 Å formed mainly by the bimetallic interaction constrained by the bulky groups, such as *tert*-butyl substituents at the bridging dbpz site. The barrier between these two minima is small and, thus, accessible at room temperature. Upon excitation of **5b**, the motion of the Pt-fragment takes place exergonically in the triplet manifold, so that the diplatinum framework easily relaxes into the ^{3}LMMCT excited state, resulting in a unique, structureless excimer emission (see Figures 5 and 10 and S5 in the Supporting Information). As for complexes **3b** and **4b**, upon geometry optimization, the two local minima in the T_1 state are located at ~3.0 and ~3.6 Å, respectively; the energy of the normal species is more or less the same as that of the excimer state (^{3}LMMCT, see Figures 11 and S6 in the Supporting Information). Moreover, the barrier for the excimer formation in the triplet manifold is calculated to be as small as ~1.0 kcal/mol, showing equilibrium between the normal and the excimer species in the lowest-lying triplet state. Finally, it is also noteworthy that no intramolecular Pt–Pt dimer formed along the ground-state (S_0) potential energy surface for **3b** and **4b** (see Figure S7 in the Supporting Information), consistent with the spectroscopic observation.

Conclusion

In summary, a series of mono- and dinuclear Pt(II) complexes, **a** and **b**, that possess a tridentate fpbpy chelate, together with either a terminal or bridging pyrazolate ligand, were designed and synthesized. All these Pt(II) complexes

(27) Kim, D.; Brédas, J.-L. *J. Am. Chem. Soc.* **2009**, *131*, 11371.
(28) (a) Grimme, S. *J. Comput. Chem.* **2004**, *25*, 1463. (b) Grimme, S. *J. Comput. Chem.* **2006**, *27*, 1787. (c) Jurecka, P.; Cerny, J.; Hobza, P.; Salahub, D. R. *J. Comput. Chem.* **2007**, *28*, 555. (d) Cerny, J.; Jurecka, P.; Hobza, P.; Valdes, H. *J. Phys. Chem. A* **2007**, *111*, 1146.
(29) Tao, J.; Perdew, J. P.; Staroverov, V. N.; Scuseria, G. E. *Phys. Rev. Lett.* **2003**, *91*, 146401.

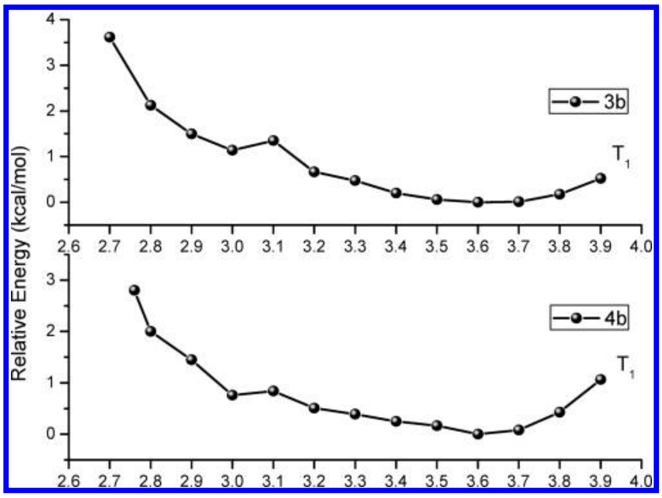

Figure 11. Potential energy surface scan of the T_1 states for complexes **3b** and **4b** versus the Pt···Pt distance. The geometries of the T_1 states were performed with the unrestricted TPSS method at each Pt···Pt distance. Note that in each scan, except for the fixed Pt···Pt distance, all other ligands are freely optimized.

exhibited bright emissive in a CH_2Cl_2 solution at room temperature. For the mononuclear **3a**, incorporation of parent pyrazolate gave a planar molecular structure, while the other functionalized pyrazolate favored a perpendicular ligand orientation. Thus, the lowest-energy excitation of monomeric **6a** is mainly assigned to the intraligand $\pi-\pi^*$ transition localized on the fpbpy ligand, together with a small proportion of a MLCT d_π(Pt) → π^*(fpbpy) transition, whereas **3a** reveals mixed MLCT (d_π(Pt) → π^*(fpbpy)) and LLCT (π(pz) → π^*(fpbpy)) transitions, giving rise to a broad and structureless emission that is different from the vibronic structured emission rendered by **6a**.

Similarly, functionalization of pyrazolate linkers in the dinuclear complexes **b** also affects their photophysical behaviors in response to the ligand-induced variation of the intramolecular Pt···Pt distance. Complexes **3b** and **4b** possess longer Pt···Pt contact and reveal dual phosphorescences originating from both the intraligand $\pi-\pi^*$ transition and the LMMCT excimer transition. Upon employing the bulky dbpz ligand, only the lower energy LMMCT emission was resolved for **5b** at RT, indicating its great exergonic excimer formation due to the strengthening of the Pt···Pt interaction and the proper orientation of the aromatic moieties to form the notable $\pi-\pi$ interaction. It is believed that coexistence of such dual phosphorescent signals could account for the various vapoluminescent and solvatochromic responses of many Pt(II) complexes, for which the solvent vapor would lead to the reversible switching of the excited-state characters from the intraligand $\pi-\pi^*$, MLCT, and even to the LMMCT transitions in the fluid and/or the solid states.[30] Moreover, observation of dual phosphorescence in solution has been recently documented, for which the higher energy band that appeared as shoulders in the spectrum is derived from a metal-perturbed, intraligand $\pi-\pi^*$ transition, while the lower energy absorption is sensitive to both of its structures and solvents, originating from an admixture of the MLCT and LLCT excited states.[31] Overall, the present studies demonstrate that the judicious selection of pyrazolate ligands, which have substituents with distinctive spatial and electronic properties, could readily lead to remarkable tuning of their structural and photophysical properties.

Experimental Section

General Information and Materials. All reactions were performed under a nitrogen atmosphere using anhydrous solvents or solvents treated with an appropriate drying reagent. Commercially available reagents were used without further purification unless otherwise stated. Mass spectra were obtained on a JEOL SX-102A instrument operating in an electron impact (EI) mode or a fast atom bombardment (FAB) mode. ^{1}H and ^{19}F NMR spectra were recorded on a Varian Mercury-400 or an INOVA-500 instrument. Elemental analyses were conducted at the NSC Regional Instrumentation Center at the National Chiao Tung University. Pyrazole (pzH) and 3,5-dimethylpyrazole (dmpzH) were commercially available (Acros). The precursor compounds Pt(fpbpy)Cl (**1**) and [Pt(fpbpy)(NCMe)](BF_4) (**2**) were prepared according to the literature method.[15] 3,5-di-*tert*-butylpyrazole (dbpzH) and 3,5-di(trifluoromethyl)-pyrazole (dtfpzH) were prepared via the reaction of 2,2,6,6-tetramethyl-3,5-heptanedione or 1,1,1,5,5,5-hexafluoro-2,4-pentanedione with hydrazine hydrate in ethanol solution.

Pt(fpbpy)(pz) (3a). A mixture of **1** (65 mg, 0.125 mmol), pyrazole (pzH) (17 mg, 0.25 mmol), and Na_2CO_3 (27 mg, 0.26 mmol) in ethanol (10 mL) was refluxed overnight, giving a yellow precipitate. After cooling the suspension to room temperature, the precipitate was filtered, washed with water and diethyl ether in sequence, and dried under vacuum; yield: 62 mg, 0.109 mmol, 87%. Single crystals suitable for X-ray diffraction study were obtained by laying a hexane solvent over the acetone solution of **3a**.

Spectral data of **3a**: MS (FAB, ^{195}Pt): *m*/*z* 551 (M^+). ^{1}H NMR (400 MHz, DMSO-d_6, 298 K): δ 10.54 (d, 1H, J_{HH} = 4.4 Hz), 8.44 (d, 2H, J_{HH} = 7.6 Hz), 8.35 (ddd, 1H, J_{HH} = 6.4, 1.5 Hz), 8.19 (d, 2H, J_{HH} = 8.8 Hz), 7.98 (t, 1H, J_{HH} = 4.4 Hz), 7.89 (dtd, 1H, J_{HH} = 7.0 Hz), 7.52 (d, 1H, J_{HH} = 1.2 Hz), 7.33 (s, 1H), 6.17 (t, 1H, J_{HH} = 1.8 Hz). ^{19}F NMR (470 MHz, DMF-d_7, 298 K): δ −60.48 (s, 3F). Anal. calcd for $C_{17}H_{11}F_3N_6Pt \cdot H_2O$: C, 35.86; H, 2.30; N, 14.76. Found: C, 36.09; H, 2.22; N, 14.16.

[{Pt(fpbpy)}$_2$(μ-pz)](BF_4) (3b). A mixture of **2** (29 mg, 0.047 mmol) and **3a** (26 mg, 0.047 mmol) in anhydrous acetonitrile (20 mL) was refluxed for 18 h. After it was cooled to room temperature, an orange solution was afforded by filtration, and the volume of extract was reduced to ~2 mL. Addition of diethyl ether yielded orange solids, which were recrystallized by slow diffusion of diethyl ether into acetonitrile; yield: 40 mg, 0.0356 mmol, 75%.

Spectral data for **3b**: MS (FAB, ^{195}Pt): *m*/*z* 1035 (M^+). ^{1}H NMR (500 MHz, CD_3CN, 298 K): δ 8.06−8.02 (m, 6H), 7.99 (d, 2H, J_{HH} = 5.5 Hz), 7.96 (d, 2H, J_{HH} = 8.0 Hz), 7.75 (d, 2H, J_{HH} = 8.5 Hz), 7.62 (d, 2H, J_{HH} = 7.0 Hz), 7.14 (dt, 2H, J_{HH} = 4.5, 2.0 Hz), 6.93 (s, 2H), 6.79 (t, 1H, J_{HH} = 2.3 Hz). ^{19}F NMR (470 MHz, acetone-d_6, 298 K): δ −61.23 (s, 6F, CF_3), −151.80 (s, 4F, BF_4). Anal. calcd for $C_{31}H_{19}BF_{10}N_{10}Pt_2$: C, 33.17; H, 1.71; N, 12.48. Found: C, 33.14; H, 2.22; N, 12.04.

Pt(fpbpy)(dmpz) (4a). An ethanol solution of **1** (13 mg, 0.025 mmol), 3,5-dimethylpyrazole (dmpzH) (24 mg, 0.3 mmol), and Na_2CO_3 (6 mg, 0.06 mmol) was stirred at room temperature overnight. Then the solvent was evaporated under vacuum, and the residue was separated by silica gel thin layer chromatography (CH_2Cl_2: MeCN = 9: 1), giving unreacted **1** (4 mg, 0.007 mmol), **4a** (4 mg, 0.007 mmol), and **4b** (3 mg, 0.003 mmol)

(30) (a) Buss, C. E.; Anderson, C. E.; Pomije, M. K.; Lutz, C. M.; Britton, D.; Mann, K. R. *J. Am. Chem. Soc.* **1998**, *120*, 7783. (b) Buss, C. E.; Mann, K. R. *J. Am. Chem. Soc.* **2002**, *124*, 1031. (c) Pomestchenko, I. E.; Castellano, F. N. *J. Phys. Chem. A* **2004**, *108*, 3485.

(31) Tam, A. Y.-Y.; Lam, W. H.; Wong, K. M.-C.; Zhu, N.; Yam, V. W.-W. *Chem.—Eur. J.* **2008**, *14*, 4562.

Table 3. Crystal Data and Refinement Parameters for Complexes **3a**, **6a**, **4b** and **5b**

	3a	**6a**	**4b**/$PF_6 \cdot C_3H_6O \cdot H_2O$	**5b**/$CF_3SO_3 \cdot C_6H_{14} \cdot H_2O$
empirical formula	$C_{17}H_{11}F_3N_6Pt$	$C_{19}H_9F_9N_6Pt$	$C_{36}H_{31}F_{12}N_{10}O_2PPt_2$	$C_{46}H_{51}F_9N_{10}O_4Pt_2S$
formula weight	551.41	687.41	1284.86	1401.21
temperature, K	220(2)	150(2)	150(2)	150(2)
crystal system	triclinic	monoclinic	monoclinic	monoclinic
space group	$P\bar{1}$	$P2_1/c$	$P2_1/c$	$P2_1/c$
a, Å	7.3716(4)	8.0916(6)	12.9340(5)	13.9608(7)
b, Å	9.7069(5)	14.4245(10)	21.6277(11)	32.3184(14)
c, Å	11.7654(6)	18.0577(12)	14.8760(6)	12.8903(6)
α, °	79.286(1)	90	90	90
β, °	84.963(1)	102.310(2)	101.512(2)	109.130(1)
γ, °	81.353(1)	90	90	90
volume, Å^3	816.25(7)	2059.2(2)	4077.6(3)	5494.8(4)
Z	2	4	4	4
ρ_{calcd}, g cm^{-3}	2.244	2.217	2.093	1.694
absorption coefficient, mm^{-1}	8.643	6.916	6.997	5.204
F(000)	520	1 296	2 448	2 728
crystal size, mm^3	0.60 × 0.10 × 0.06	0.80 × 0.30 × 0.02	0.08 × 0.05 × 0.05	0.25 × 0.25 × 0.10
reflections collected	10 661	12 933	18 450	42 155
independent reflections	3 751 [R(int) = 0.0678]	4 714 [R(int) = 0.0539]	7 172 [R(int) = 0.0686]	12 614 [R(int) = 0.0686]
max., min. transmission	0.6251, 0.0784	0.8741, 0.0723	0.717, 0.631	0.6242, 0.3562
data/restraints/parameters	3 751/0/271	4 714/0/352	7 172/0/572	12 614/9/611
goodness-of-fit on F^2	1.006	1.137	1.044	1.114
final R indices [$I > 2\sigma(I)$]	R_1 = 0.0363, wR_2 = 0.0717	R_1 = 0.0570, wR_2 = 0.1104	R_1 = 0.0463, wR_2 = 0.1038	R_1 = 0.0521, wR_2 = 0.1326
R indices (all data)	R_1 = 0.0414, wR_2 = 0.0733	R_1 = 0.0833, wR_2 = 0.1199	R_1 = 0.0819, wR_2 = 0.1288	R_1 = 0.0721, wR_2 = 0.1439
largest different peak and hole	2.629 and −1.652 eÅ^{-3}	1.850 and −2.295 eÅ^{-3}	1.658 and −1.852 eÅ^{-3}	1.812 and −1.117 eÅ^{-3}

in approximately 31, 27, and 22%, respectively. It is notable that **4a** was capable of partially converting to **4b** during workup. Accordingly, **4a** was never isolated as a pure sample for photophysical measurement; nevertheless, its ^{1}H NMR signals were recognized by elimination of the respective signals from **4b** and free pyrazole.

Spectra data of **4a**: ^{1}H NMR (acetone-d_6, 400 MHz) δ: 8.71 (d, 1H, J = 5.6 Hz), 8.55 (d, 1H, J = 8.4 Hz), 8.35 (t, 1H, J = 8.4 Hz), 8.26−8.20 (m, 2H), 7.93 (d, 1H, J = 7.2 Hz),7.72 (t, 1H, J = 7.2 Hz), 7.12 (s, 1H), 5.74 (s, 1H), 2.35 (s, 3H), 2.25 (s, 3H).

[{Pt(fpbpy)}$_2$(μ-dmpz)](PF$_6$) (4b). A mixture of **1** (30 mg, 0.058 mmol), 3,5-dimethylpyrazole (dmpzH) (12 mg, 0.12 mmol), and Na_2CO_3 (13 mg, 0,12 mmol) in ethanol (15 mL) was refluxed overnight to give a yellow solution. After the solution was cooled to room temperature, solid KPF_6 (0.1 g, 0.57 mmol) was added, and the mixture was stirred again for 5 h. Then the mixture was evaporated to dryness, and the product was extracted with CH_2Cl_2. Yellow crystals of **4b** were obtained by laying hexane over this CH_2Cl_2 solution; yield: 32 mg, 0.026 mmol, 91%.

Spectral data of **4b**: MS (FAB, ^{195}Pt): m/z 1063 (M$^+$). ^{1}H NMR (500 MHz, acetone-d_6, 298 K): δ 8.30−8.21 (m, 8H), 8.09 (d, 2H, J_{HH} = 8.0 Hz), 7.93 (d, 2H, J_{HH} = 8.5 Hz), 7.28 (dt, 2H, J_{HH} = 6.5, 1.5 Hz), 7.13 (s, 2H), 6.44 (s, 1H), 2.57 (s, 6H). ^{19}F NMR (470 MHz, acetone-d_6, 298 K): δ −61.18 (s, 6F, CF_3), −72.58 (d, 6F, PF_6, J_{PF} = 707 Hz). Anal. calcd for $C_{33}H_{23}F_{12}N_{10}PPt_2$: C, 32.79; H, 1.92; N, 11.59. Found: C, 32.50; H, 2.21; N, 11.54.

Pt(fpbpy)(dbpz) (5a). A mixture of **1** (52 mg, 0.10 mmol), 3,5-di-*tert*-butylpyrazole (dbpzH) (36 mg, 0.20 mmol), and Na_2CO_3 (22 mg, 0.21 mmol) in ethanol (25 mL) was refluxed overnight to give a clear yellow solution, which was evaporated to dryness. The product was extracted with CH_2Cl_2, and the volume of extract was reduced to ~3 mL. Addition of hexane to this CH_2Cl_2 solution yielded an orange-yellow solid, which was further recrystallized by slow diffusion of hexane into CH_2Cl_2 solution; yield: 45 mg, 0.068 mmol, 68%. Similar to its methyl-substituted analogue **4a**, **5a** was found to partially convert to its dimeric species **5b** during workup, so its analytical analysis and photophysical measurement were not recorded.

Spectral data of **5a**: ^{1}H NMR (500 MHz, CD_3CN, 298 K): δ 8.13 (m, 2H), 8.02 (t,1H, J_{HH} = 8.0 Hz), 7.95 (d, 1H, J_{HH} = 7.0 Hz), 7.76 (d, 1H, J_{HH} = 7.0 Hz), 7.47 (q, 1H, J_{HH} = 5.0 Hz), 7.01 (s, 1H), 6.92 (d, 1H, J_{HH} = 6.0 Hz), 6.01 (s, 1H), 1.41 (s, 9H), 1.32 (s, 9H). ^{19}F NMR (470 MHz, CD_3CN, 298 K): δ −61.47 (s, 3F).

[{Pt(fpbpy)}$_2$(μ-dbpz)](BF$_4$) (5b). A mixture of **2** (25 mg, 0.041 mmol) and **5a** (27 mg, 0.041 mmol) in anhydrous acetonitrile (20 mL) was refluxed for 18 h. After cooling to room temperature, an orange solution was filtered, and the volume of filtrate was reduced to ~2 mL. Addition of diethyl ether into this acetonitrile solution yielded an orange powder, which was further recrystallized by slow diffusion of diethyl ether into acetonitrile; yield: 33 mg, 0.027 mmol, 65%. Initial attempts to grow single crystals of **5b** for X-ray structural analysis unfortunately failed. However, single crystals of a metathetical compound, denoted as [{Pt(fpbpy)}$_2$(μ-dbpz)](CF_3SO_3) (**5b**), were obtained from treatment of **5a** with [Pt(fpbpy)(NCMe)]-(CF_3SO_3), followed by a slow recrystallization from a mixture of CH_2Cl_2 and hexane at room temperature.

Spectral data of **5b**: MS (FAB, ^{195}Pt): m/z 1147 (M$^+$). ^{1}H NMR (500 MHz, CD_3CN, 298 K): δ 8.00−8.07 (m, 4H), 7.91 (d, 2H, J_{HH} = 8.5 Hz), 7.82 (d, 2H, J_{HH} = 5.0 Hz), 7.72 (d, 2H, J_{HH} = 7.5 Hz), 7.58 (d, 2H, J_{HH} = 8.5 Hz), 7.33 (t, 2H, J_{HH} = 6.5 Hz), 6.79 (s, 2H), 6.56 (s, 1H), 1.53 (s, 18H). ^{19}F NMR (470 MHz, CD_3CN, 298 K): δ −60.96 (s, 6F, CF_3), −151.79 (s, 4F, BF_4). Anal. calcd for $C_{39}H_{35}BF_{10}N_{10}Pt_2$: C, 37.94; H, 2.86; N, 11.34. Found: C, 37.69; H, 3.28; N, 11.03.

Pt(fpbpy)(dtfpz) (6a). A mixture of **1** (60 mg, 0.115 mmol), 3,5-di(trifluoromethyl)pyrazole (dtfpzH) (16 mg, 0.24 mmol), and Na_2CO_3 (25 mg, 0.24 mmol) in ethanol (10 mL) was refluxed for 12 h. This Pt(II) monomer was precipitated from the reaction mixture, which was collected and dried under vacuum; yield: 69 mg, 0.098 mmol, 85%. Single crystals suitable for X-ray diffraction study were obtained by laying hexane over the CH_2Cl_2 solution of **5** at room temperature.

Spectral data of **6a**: MS (FAB, ^{195}Pt): m/z 688 (M$^+$). ^{1}H NMR (400 MHz, DMSO-d_6, 298 K): δ 8.59 (d, 1H, J_{HH} = 7.2 Hz), 8.43 (ddd, 1H, J_{HH} = 6.6, 1.5 Hz), 8.31−8.39 (m, 2H), 8.10 (dd, 1H, J_{HH} = 6.4, 1.2 Hz), 7.80 (dtd, 1H, J_{HH} = 4.4, 1.8, 1.2 Hz), 7.51 (d, 1H, J_{HH} = 4.8 Hz), 7.35 (s, 1H), 7.25 (s, 1H). ^{19}F NMR (470 MHz, DMF-d_7, 298 K): δ −55.44 (s, 3F, fpbpy), −57.96 (s, 3F, bfpz), −58.23 (s, 3F, bfpz). Anal. calcd for $C_{19}H_9F_9N_6Pt \cdot H_2O$: C, 32.35; H, 1.57; N, 11.91. Found: C, 32.46; H, 1.54; N, 11.79.

X-ray Diffraction Studies. Single-crystal X-ray diffraction data of **3a**, **6a**, **4b**, and **5b** were measured on a Bruker SMART

Apex CCD diffractometer using (Mo−K_α) radiation (λ = 0.71073 Å). Data were collected with the SMART program. Cell refinement and data reduction were performed with the SAINT program. The structure was determined using the SHELXTL/PC program and refined using full-matrix least-squares,[32] for which their crystallographic refinement parameters are summarized in Table 3.

Computational Methodology. DFT calculations on the electronic singlet and triplet states of complexes **a** and **b** were carried out using a hybrid Hartree−Fock/density functional model (PBE1PBE) based on the Perdew−Burke−Erzenrhof (PBE) functional.[33] A double-ζ quality basis set, consisting of Hay and Wadt's effective core potentials (LANL2DZ),[34] was employed for the Pt atom, and a 6-31G* basis set was employed for the H, C, N, and F atoms, while a relativistic effective core potential (ECP) was applied to the inner core electrons of Pt atoms. TD-DFT calculations[35] for the $S_0 \rightarrow S_n$ and $T_1 \rightarrow S_0$ transitions using the PBE1PBE functional were then performed based on the optimized geometries at the S_0 and T_1 states. Restricted and unrestricted formalisms were adopted in the singlet and triplet geometry optimization calculations, respectively. To consider the solvation effect, the results were then combined with an integral equation formalism-polarizable continuum model (IEF-PCM, in dichloromethane), implemented in Gaussian 03.[36] Typically,the 10 lowest triplet and singlet roots of the nonhermitian eigenvalue equations were obtained to determine the vertical excitation energies. Oscillator strengths were deduced from the dipole transition-matrix elements (for singlet states only). All calculations were carried out using Gaussian 03.[37]

Acknowledgment. This work was supported by the National Science Council of Taiwan. We are also grateful to the National Center for High-Performance Computing for computer time and facilities.

Supporting Information Available: X-ray crystallographic data file (CIF) of the studied complexes **3a**, **6a**, **4b**, and **5b**. This material is available free of charge via the Internet at http://pubs.acs.org.

(32) (a) Sheldrick, G.-M. *SHELXL97, Program for the refinement of crystal structure*; University of Göttingen: Göttingen, Germany, 1997; (b) *SHELXTLV6.1*; BrukerAXS, Inc: Madison, WI, 2000.

(33) (a) Perdew, J. P.; Burke, K.; Ernzerhof, M. *Phys. Rev. Lett*. **1996**, *77*, 3865. (b) Perdew, J. P.; Burke, K.; Ernzerhof, M. *Phys. Rev. Lett*. **1997**, *78*, 1396. (c) Adamo, C.; Barone, V. *J. Chem. Phys*. **1999**, *110*, 6158.

(34) (a) Hay, P. J.; Wadt, W. R. *J. Chem. Phys*. **1985**, *82*, 270. (b) Wadt, W. R.; Hay, P. J. *J. Chem. Phys*. **1985**, *82*, 284. (c) Hay, P. J.; Wadt, W. R. *J. Chem. Phys*. **1985**, *82*, 299.

(35) (a) Jamorski, C.; Casida, M. E.; Salahub, D. R. *J. Chem. Phys*. **1996**, *104*, 5134. (b) Petersilka, M.; Grossmann, U. J.; Gross, E. K. U. *Phys. Rev. Lett*. **1996**, *76*, 1212. (c) Bauernschmitt, R.; Ahlrichs, R.; Hennrich, F. H.; Kappes, M. M. *J. Am. Chem. Soc*. **1998**, *120*, 5052. (d) Casida, M. E. *J. Chem. Phys*. **1998**, *108*, 4439. (e) Stratmann, R. E.; Scuseria, G. E.; Frisch, M. J. *J. Chem. Phys*. **1998**, *109*, 8218.

(36) Cancès, M. T.; Mennucci, B.; Tomasi, J. *J. Chem. Phys*. **1997**, *107*, 3032.

(37) Frisch, M. J.; Trucks, G. W.; Schlegel, H. B.; Scuseria, G. E.; Robb, M. A.; Cheeseman, J. R.; Montgomery, J. A., Jr.; Vreven, T.; Kudin, K. N.; Burant, J. C.; Millam, J. M.; Iyengar, S. S.; Tomasi, J.; Barone, V.; Mennucci, B.; Cossi, M.; Scalmani, G.; Rega, N.; Petersson, G. A.; Nakatsuji, H.; Hada, M.; Ehara, M.; Toyota, K.; Fukuda, R.; Hasegawa, J.; Ishida, M.; Nakajima, T.; Honda, Y.; Kitao, O.; Nakai, H.; Klene, M.; Li, X.; Knox, J. E.; Hratchian, H. P.; Cross, J. B.; Bakken, V.; Adamo, C.; Jaramillo, J.; Gomperts, R.; Stratmann, R. E.; Yazyev, O.; Austin, A. J.; Cammi, R.; Pomelli, C.; Ochterski, J. W.; Ayala, P. Y.; Morokuma, K.; Voth, G. A.; Salvador, P.; Dannenberg, J. J.; Zakrzewski, V. G.; Dapprich, S.; Daniels, A. D.; Strain, M. C.; Farkas, O.; Malick, D. K.; Rabuck, A. D.; Raghavachari, K.; Foresman, J. B.; Ortiz, J. V.; Cui, Q.; Baboul, A. G.; Clifford, S.; Cioslowski, J.; Stefanov, B. B.; Liu, G.; Liashenko, A.; Piskorz, P.; Komaromi, I.; Martin, R. L.; Fox, D. J.; Keith, T.; Al-Laham, M. A.; Peng, C. Y.; Nanayakkara, A.; Challacombe, M.; Gill, P. M. W.; Johnson, B.; Chen, W.; Wong, M. W.; Gonzalez, C.; Pople, J. A. *Gaussian 03*, revision C.02; Gaussian, Inc.: Wallingford, CT, 2004.